Estimation-based Robust Switching Control of a DC-DC Boost Converter

Saif Ahmad, Ryan de Souza, Pauline Kergus, Zohra Kader, Stéphane Caux

Estimation-based Robust Switching Control of a DC-DC Boost Converter

Saif Ahmad Ryan P. C. de Souza Pauline Kergus Zohra Kader Stéphane Caux

***Abstract*—In this work, a robust switching control design technique is presented for a DC-DC boost converter. It allows operation under uncertain equilibrium conditions arising due to perturbations in the input and load parameters. A parameter estimator is designed to update the equilibrium point for the switching controller in real-time. In order to mitigate the noise amplification problem associated with the designed parameter estimator, the estimation error injection term is filtered to obtain the desired level of noise suppression in the final set of estimates. To demonstrate the efficiency of the developed scheme, the proposed control design is validated in simulation as well as on an experimental platform, and compared to PWM-based state-feedback control with integral action.**

***Index Terms*—DC-DC boost converter, switching control, electric vehicle charging, parameter estimation, measurement noise.**

I. Introduction

This paper deals with the problem of robust global stabilization of switching power converters. It is an extension of the work presented in [1], which can be considered as a preliminary version. As recalled in [2], the projected increase in the number of DC-powered components and distributed sources that generate DC power, DC microgrids are a good candidate for future energy systems. In order to meet the expectations regarding the performance of such DC microgrids, efficient control and energy management are required at each control level, which makes DC-DC converter control of crucial importance.

In this context, a number of linear control strategies have been proposed in the literature based on averaged small signal models of DC-DC converters [3], [4] Such control techniques ensure desired nominal performance and system stability but only in the neighborhood of the equilibrium point, which is not known usually. Power converters are generally characterized by highly nonlinear dynamics and continuous parametric variations subject to source and load conditions, which in turn shift the equilibrium point [5]. This highlights the limitations of closed-loop performance achievable via linear feedback control and the need for more advanced control strategies in this area that account for the switching and parameter-varying nature of converters. Advanced control methods for DC-DC converters in DC microgrids are reviewed in [6] and classified into the following categories: model predictive control, backstepping, sliding mode control (SMC), passivity-based control, observer/estimation-based technique, and intelligent control. More recently, principles of switched systems theory have been successfully employed as an alternative to the averaging approach for control of power converters in [7]. One of the main advantages of using switched systems theory is that linearization around the equilibrium is not required, and global stabilization can be ensured. The main drawback of the switching controller in [7] is that it is designed for a constant equilibrium point. This problem has recently been addressed for DC-DC power converters by using augmented state observer [8] and state augmentation via tracking error integral [9]. In [1], the problem of uncertain equilibrium in the context of switching control designed for a DC-DC boost converter (DBC) is tackled by estimating the uncertain parameters. Unlike [8], the estimator designed in [1] approximates only the required unknown parameters and not the measurable states. Moreover, the noise amplification problem commonly associated with observers/estimators (such as those used in [8]) is addressed by the estimation error filtering approach introduced in [10], which results in better estimation quality and allows the freedom to introduce a desired level of filtering in the obtained estimates. In addition, the resulting estimation error dynamics are devoid of switched terms which in turn facilitates the tuning of the estimator, and gives simpler *linear matrix inequality* (LMI) conditions for the stability of the designed estimator. Furthermore, the robust switched control algorithm is implemented via a hysteresis block, providing a simple and intuitive solution to the infinite switching frequency problem [7] and facilitating practical implementation.

The novelty of this work resides in the implementation and experimental validation of a robust switching controller. It should be noted that, to our knowledge, implementations and experimental validations of hybrid control laws on converters, such as the one presented in this paper, remain fairly rare [11] [12] [13] [14] [15] despite promising results. Indeed, the presented switching control technique is relevant for various industrial applications as it guarantees stability for any equilibrium point that can vary in a user-specified range of operations. Switching control paradigms, as the one presented in our work, remain rarely applied by power electronics specialists,

Ryan P.C. de Souza, Pauline Kergus, Zohra Kader and StÃ©phane Caux are affiliated to LAPLACE (Université de Toulouse, CNRS, INPT, UPS), Toulouse, France.
Saif Ahmad is with LIS (UMR CNRS 7020), Marseille, France.
email: {pitanga, kergus, kader, caux}@laplace.univ-tlse.fr, saif.ahmad@lis-lab.fr
This work is funded by ADEME, the French Agency for Ecological Transition, as part of the I-REVE project.

978-1-6654-9071-9/23/$31.00 ©2023 IEEE

who mainly use well-established techniques based on the use of averaged and continuous models [16]. At the same time, switching control is currently a very active field of research in the automatic control community. The idea of this paper is to transfer this method between both communities and to provide practitioners insights regarding the tuning knobs for successful implementation. Furthermore, another novelty of our work lies in developing a noise-suppressing parameter estimator for switched systems which allows us to consider all types of linear internal models. Hence, if the actual parameter variation can be perfectly modeled through a system of linear equations, we can guarantee asymptotic convergence in the absence of measurement noise. Even in the case of a mismatch, a practical convergence can be ensured close to the origin via a sufficiently high estimator parameter. This is in contrast to most existing techniques such as in [17], [18] which are limited to the assumption of slow variation in the parameters and cannot account for other forms of variation in the parameters such as linearly varying with time, sinusoidal, etc. In addition, we highlight the problem of noise amplification in the switched parameter estimator and present a modular redesign approach that allows a user-defined level of noise filtering in the obtained estimate via a bank of low-pass filters. This is also in contrast to the approaches covered in literature which mostly ignore the problem of noise amplification in parameter estimators. It is also to be noted that the proposed parameter estimator has a general structure that can be used in combination with other types of controllers as well. In comparison with the previous work presented in [1], an experimental validation of the developed robust switching control algorithm is incorporated and additional considerations regarding parameter estimation performance are provided. Rigorous stability analysis of the designed parameter estimator is presented under the effect of residual term and measurement noise. Furthermore, we analyze the noise-suppressing feature of the proposed estimator in comparison to the normal switched parameter estimator.

In order to situate the proposed method among other advanced techniques, it should be noted that it is based on the estimation of parameter variations at the current time step while model predictive control (MPC) needs a prediction model valid over its whole horizon. MPC also comes with a higher numerical complexity as optimization is performed on a longer horizon compared to the proposed switching control. When it comes to sliding mode control, the sliding surface is usually computed based on a linearized model and as for traditional PWM control, stability is then only guaranteed around the corresponding operating condition. Hysteresis can be used in addition to the sliding mode control as done in the proposed work.

This paper is organized as follows. Section II first introduces the switching model for boost converters and highlights the importance of considering variations of operating points in the control design of DC-DC converters. Section III then recalls the proposed control and estimation algorithm from [1], along with the hysteresis and noise filtering approach to facilitate practical implementation along with stability and frequency domain analysis. The efficiency of the proposed approach is then illustrated in Section IV through numerical simulations, experimental validation and comparison with PWM-based control. The paper concludes in Section V with a summary of the results and future research directions.

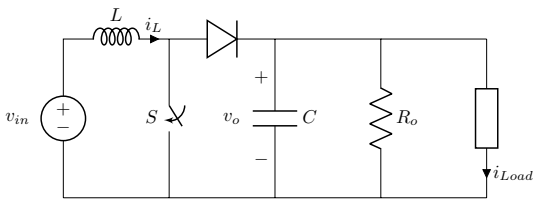

Fig. 1: Circuit of a DC-DC boost converter.

Notations: $\boldsymbol{I_n}$ is an identity matrix of dimension $n \times n$, $\mathbf{0}$ is a zero vector or matrix of appropriate dimension, $\text{diag}(a_1, \ldots, a_n)$ denotes a diagonal matrix with $a_1, \ldots, a_n$ as diagonal elements. Given a symmetric matric $\mathbf{M}$, $\mathbf{M} \prec \mathbf{0}$ (resp. $\mathbf{M} \preceq \mathbf{0}$) means that $\mathbf{M}$ is negative-definite (resp. negative-semidefinite). The notation for positive-(semi)definiteness is analogous. For a vector $\boldsymbol{x} \in \mathbb{R}^n, \|\boldsymbol{x}\| = \sqrt{\boldsymbol{x^T x}}$ denotes the $\boldsymbol{L^2}$ or Euclidean norm whereas for a matrix $\boldsymbol{A} \in \mathbb{R}^{m \times n}, \|\boldsymbol{A}\| = \sup_{x \neq 0} \frac{\|\boldsymbol{Ax}\|}{\|\boldsymbol{x}\|}$ is the induced matrix norm. Similarly, $\|x\|_\infty$ for a vector $x \in \mathbb{R}^n$ is defined as $\max\{|x_1|, |x_2|, \ldots, |x_n|\}$. A function $f(x) : \mathbb{R}_{\geq 0} \to \mathbb{R}_{\geq 0}$ belongs to class $\mathcal{K}$ when it is continuous, strictly increasing and $f(0) = 0$.

II. Problem Formulation

The electric circuit of the considered DBC is shown in Fig. 1, where L is the inductance, C is the capacitance, R_o is a load resistance, i_L is the inductor current, v_o is the output voltage, v_{in} is the input voltage, and i_{Load} is the current being supplied to another variable load connected in parallel.

The variable $\sigma \in \{0, 1\}$ represents the state of the switching device S in the following way: $\sigma = 1$ (resp. $\sigma = 0$) when S is in the on (resp. off) state. The instantaneous model can then be written as follows:

$$\dot{\boldsymbol{x}}(t) = \boldsymbol{A_\sigma x}(t) + \boldsymbol{G p}(t), \tag{1}$$

where $\boldsymbol{x}(t) := [i_L(t) \;\; v_o(t)]^T$ denotes the system state, $\boldsymbol{p}(t) = [p_1(t), p_2(t)]^T := [v_{in}(t) \;\; i_{Load}(t)]^T$ is the parameter vector, and matrices $\boldsymbol{A_\sigma}$, with $\sigma \in \{0, 1\}$, and $\boldsymbol{G}$ are given by:

$$\boldsymbol{A_\sigma} = \begin{bmatrix} 0 & -\frac{(1-\sigma)}{L} \\ \frac{(1-\sigma)}{C} & -\frac{1}{R_o C} \end{bmatrix}, \quad \boldsymbol{G} = \begin{bmatrix} \frac{1}{L} & 0 \\ 0 & -\frac{1}{C} \end{bmatrix}. \tag{2}$$

The possible equilibrium points of dynamics (1) are the same as those of the nonlinear averaged model [8]:

$$\dot{\boldsymbol{x}}(t) = \boldsymbol{A}(\bar{\sigma})\boldsymbol{x}(t) + \boldsymbol{G p}(t), \tag{3}$$

where $\boldsymbol{A}(\bar{\sigma}) := \bar{\sigma}\boldsymbol{A_1} + (1 - \bar{\sigma})\boldsymbol{A_0}$ and $\bar{\sigma} \in [0, 1]$. A point $\boldsymbol{x}^* = [i_L^\star \;\; v_o^\star]^T$ is an equilibrium of (3) if there exists some $\bar{\sigma}^* \in [0, 1]$ such that $\boldsymbol{A}(\bar{\sigma}^*)\boldsymbol{x}^* + \boldsymbol{G p} = \mathbf{0}$. The value of $\bar{\sigma}^*$ then corresponds to the steady-state duty cycle of the converter.

The control objective in this paper is the stabilization of the output voltage at a desired value $v_o^\star$. Assuming $0 < \bar{\sigma}^* < 1$, the equilibrium point $\boldsymbol{x}^*$ around which the system will stabilize for a given parameter vector $\boldsymbol{p}$ satisfies

$$\boldsymbol{A}(\bar{\sigma}^*)\boldsymbol{x^*(p)} + \boldsymbol{Gp} = 0, \tag{4}$$

where the dependence of the equilibrium on $\boldsymbol{p}$ has been made explicit.

III. Robust Switching Control Design

In Section III-A, the proposed switching control strategy ensuring global stabilization of a given equilibrium point is presented. It is based on the instantaneous model expressed in (1). Then, in Section III-B, the estimation paradigm used in this work is developed. The estimator and switching controller are connected in Section III-C. A scheme providing a global view of the entire closed-loop system is shown in Fig. 2.

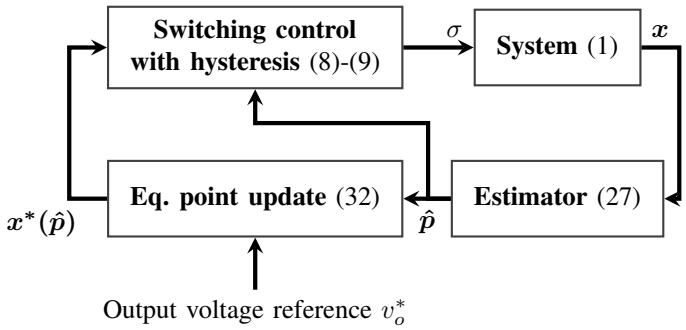

Fig. 2: Global view of the closed-loop system and the considered control architecture.

A. Switching Controller with hysteresis

For a given equilibrium $\boldsymbol{x^*(p)}$, the classical quadratic Lyapunov candidate $V(\boldsymbol{x}-\boldsymbol{x^*(p)}) = (\boldsymbol{x}-\boldsymbol{x^*(p)})^T\boldsymbol{P}(\boldsymbol{x}-\boldsymbol{x^*(p)})$ is considered, with $\boldsymbol{P} = \boldsymbol{P}^T \succ 0$. In order to guarantee that $\boldsymbol{x^*(p)}$ is a globally asymptotically stable equilibrium of system (1) towards which $\boldsymbol{x}(t)$ converges with a minimal decay rate $\alpha > 0$, one wants to ensure that $\dot{V}(\boldsymbol{x}-\boldsymbol{x^*(p)}) \leq \alpha(\boldsymbol{x}-\boldsymbol{x^*(p)})^T(\boldsymbol{x}-\boldsymbol{x^*(p)})$. The derivation of $\dot{V}$, as done in [19] leads to the following sufficient condition: if there exists $\boldsymbol{P} = \boldsymbol{P}^T \succ 0$ such that the following Linear Matrix Inequality (LMI) is satisfied:

$$\boldsymbol{A}^T(\bar{\sigma}^*)\boldsymbol{P} + \boldsymbol{P}\boldsymbol{A}(\bar{\sigma}^*) + 2\alpha\boldsymbol{P} \preceq \boldsymbol{0}. \tag{5}$$

then the $\boldsymbol{x^*(p)}$ is a globally asymptotically stable equilibrium with a decay rate α.

Finding a solution to LMI (5) is a convex problem that can be efficiently solved using commercially available software (such as Matlab). A higher α ensures that the state $\boldsymbol{x}(t)$ converges faster to the equilibrium $\boldsymbol{x^*(p)}$. A necessary condition for LMI (5) to be feasible is that α should be lower than the absolute value of the real part of the rightmost eigenvalue of $\boldsymbol{A}(\bar{\sigma}^*)$. In practice, it means that the decay rate α, i.e. the speed of the controlled system, is limited by the slowest dynamics of the averaged model (3) around equilibrium.

Based on the solution $\boldsymbol{P}$ to LMI (5), the following switching controller can be built:

$$\sigma(t) \in \underset{\sigma\in\{0,1\}}{\arg\min}(\boldsymbol{x}(t) - \boldsymbol{x^*}(\boldsymbol{p}(t))^T\boldsymbol{P}(\boldsymbol{A_\sigma x}(t) + \boldsymbol{Gp}(t)) \tag{6}$$

that globally asymptotically stabilizes system (1) at $\boldsymbol{x^*(p)}$. Indeed, as originally introduced in [19], this switching rule consists of selecting the highest decrease rate at each time instant. Since in (6) the term $\boldsymbol{Gp}(t)$ does not depend on the mode σ, the controller can be equivalently expressed as:

$$\sigma(t) \in \underset{\sigma\in\{0,1\}}{\arg\min}(\boldsymbol{x}(t) - \boldsymbol{x^*}(\boldsymbol{p}(t))^T\boldsymbol{P}\boldsymbol{A_\sigma x}(t). \tag{7}$$

Unlike more traditional control methods, the switching law presented here does not require linearization around the equilibrium point and global stabilization is ensured. Furthermore, note that the controller directly provides the mode to be selected at each time instant, and thus a modulation stage between the controller and the switching device is not required.

A significant drawback of switching law (7) is the fact that it leads to the occurrence of sliding modes [19], which in practical terms means that the switching frequency rises to unacceptable high values. According to (7), switching only occurs when both modes minimize the objective function in (7). This can only occur on the surface $s(\boldsymbol{x},\boldsymbol{p}) = 0$, where:

$$s(\boldsymbol{x},\boldsymbol{p}) := (\boldsymbol{x} - \boldsymbol{x^*(p)})^T\boldsymbol{P}\boldsymbol{D}\boldsymbol{x}, \tag{8}$$

and $\boldsymbol{D} := \boldsymbol{A_1} - \boldsymbol{A_0}$.

In order to prevent the occurrence of sliding modes, a hysteresis-based strategy is employed here to bound the switching frequency at a finite value. To that end, a parameter-dependant hysteresis band $h(\boldsymbol{p}) > 0$ is introduced: as long as $|s(\boldsymbol{x},\boldsymbol{p})| < h(\boldsymbol{p})$, switching is not allowed, otherwise if $|s(\boldsymbol{x},\boldsymbol{p})| \geq h(\boldsymbol{p})$, switching is governed by the proposed controller in (7).

Assuming that the switching frequency is high compared to the system bandwidth, it can be shown [7] that the following equation expresses the relationship between the steady-state switching frequency f_s and the hysteresis parameter:

$$h(\boldsymbol{p}) = \frac{1}{2f_s}\frac{|\boldsymbol{b_0}(\boldsymbol{p})^T\boldsymbol{P}\boldsymbol{D}\boldsymbol{x^*}(\boldsymbol{p})\boldsymbol{x^*}(\boldsymbol{p})^T\boldsymbol{D}^T\boldsymbol{P}\boldsymbol{b_1}(\boldsymbol{p})|}{(|\boldsymbol{b_0}(\boldsymbol{p})^T\boldsymbol{P}\boldsymbol{D}\boldsymbol{x^*}(\boldsymbol{p})| + |\boldsymbol{b_1}(\boldsymbol{p})^T\boldsymbol{P}\boldsymbol{D}\boldsymbol{x^*}(\boldsymbol{p})|)}, \tag{9}$$

where $\boldsymbol{b_\sigma}(\boldsymbol{p}) := \boldsymbol{A_\sigma}\boldsymbol{x^*}(\boldsymbol{p}) + \boldsymbol{Gp}$, $\sigma = 0, 1$. In order to keep the switching frequency bounded at a desired value f_s, parameter $h(\boldsymbol{p})$ is then updated in real-time according to (9).

Remark 1: As stated earlier, the speed of the controlled system is limited by the slowest dynamics of the averaged model (3), compared to which the switching frequency is chosen high for properly designed converters. Therefore, the assumption that the switching frequency is high compared to the system bandwidth normally holds in practice. This assumption is also valid when using more classical PWM-based techniques: for a given switching frequency f_s, a typical choice is to operate the PWM at $f_{PWM} = f_s/10$ and the

controller is designed so that the system bandwidth is placed around $f_{PWM}/10$.

Remark 2: System (1) and switching controller (7) are not specific to DBCs. In fact, they can be used to model and control a wider class of DC-DC converters including buck, buck-boost, and flyback converters among others [8], [9]. A general methodology to model converters as switched systems such as (1) can be found in [20], laying the ground for extending the proposed method for more complex topologies. Moreover, the problem of uncertain equilibria is common to all power converters due to the inherent intermittency of the renewables and uncertain load conditions (time-varying $\boldsymbol{p}(t)$) in most applications. Thus, the presented solutions, results, and ensuing discussions are more general and can easily be extended for other converter topologies.

Note that the controller (with or without hysteresis) requires the knowledge of the equilibrium point $\boldsymbol{x^*(p(t))}$, which depends on both $p_1(t)$ and $p_2(t)$. Moreover, note that $\bar{\sigma}^*$, used in the definition of LMI (5), is also dependent on $\boldsymbol{p}$. It implies that either the measurements of source and load signals (incurring additional cost) or their real-time estimations are required to ensure accurate tracking of the uncertain and possibly time-varying equilibrium point $\boldsymbol{x^*}(\boldsymbol{p}(t))$. If the measurements are unavailable, it then becomes necessary to estimate $\boldsymbol{p}(t)$, which is the subject of the next subsection.

B. Parameter Estimator

In real-world industrial applications, $\boldsymbol{p}(t)$ is uncertain and time-varying which in turn causes the equilibrium point $\boldsymbol{x^*(p)}$ to change accordingly. Assuming that p_1 is bounded such that $v_{in}^- \leq p_1 \leq v_{in}^+ < v_o^\star$, where v_{in}^- and v_{in}^+ are specified by the user to define the range of input voltages against which the designed controller will guarantee stability. Note that if $v_{in}^+ > v_o^\star$, then the equilibrium point may be unreachable since the output voltage of a DBC cannot be lower than the input voltage. As $p_1 = v_{in}$ evolves over time, the steady-state duty cycle $\bar{\sigma}^*$ must be updated according to the following equation:

$$\bar{\sigma}^* = 1 - \frac{p_1}{v_o^\star}, \tag{10}$$

so that the desired output voltage can be tracked.

In order for the control law (7) to stabilize the equilibrium point for all possible values of $\bar{\sigma}^*$, one must find a single matrix $\boldsymbol{P} \succ \boldsymbol{0}$ such that (5) holds for all $\bar{\sigma}^* \in [\bar{\sigma}^*_{min}, \bar{\sigma}^*_{max}]$, where $\bar{\sigma}^*_{min} = 1 - v_{in}^+/v_o^\star$ and $\bar{\sigma}^*_{max} = 1 - v_{in}^-/v_o^\star$. Thanks to the convexity of (5), this is true if the following two LMIs hold:

$$\boldsymbol{A}^T(\bar{\sigma})\boldsymbol{P} + \boldsymbol{P}\boldsymbol{A}(\bar{\sigma}) + 2\alpha\boldsymbol{P} \preceq 0, \quad \bar{\sigma} \in \{\bar{\sigma}^*_{min}, \bar{\sigma}^*_{max}\}. \tag{11}$$

Remark 3: In order for (11) to be feasible, it is necessary (but not sufficient) to choose α to be lower (in magnitude) than the real part of the rightmost eigenvalue of both $\boldsymbol{A}(\bar{\sigma}^*_{min})$ and $\boldsymbol{A}(\bar{\sigma}^*_{max})$.

Remark 4: For the sake of simplicity, it is assumed in this paper that R_o is a known load resistance. However, uncertainties in this parameter can be addressed by adapting the LMIs in (11) to be solved in a similar way as in [8], for instance.

Now, in order to obtain the estimate of uncertain parameters, it is assumed that the parameter vector $\boldsymbol{p}(t)$ is generated by a known linear exo-system of the form

$$\begin{aligned} \dot{\boldsymbol{\zeta}}_{\boldsymbol{p}}(t) &= \boldsymbol{A_p}\boldsymbol{\zeta_p}(t) \\ \boldsymbol{p}(t) &= \boldsymbol{C_p}\boldsymbol{\zeta_p}(t), \end{aligned} \tag{12}$$

with $\boldsymbol{A_p} \in \mathbb{R}^{m\times m}$ and $\boldsymbol{C_p} \in \mathbb{R}^{2\times m}$, and $\boldsymbol{\zeta_p} \in \mathbb{R}^m$ the state vector of the exo-system. This assumption allows us to consider a wider class of parameter behaviors such as linearly varying with time, sinusoidal etc., or a combination of them, which arises in practical systems. Furthermore, the common assumption of $\dot{\boldsymbol{p}} = \boldsymbol{0}$ considered in [8], [9], is a special case of (12) obtained with $\boldsymbol{A_p} = \boldsymbol{0}$ and $\boldsymbol{C_p} = \boldsymbol{I_2}$. The user can then choose $\boldsymbol{A_p}$ and $\boldsymbol{C_p}$ to reflect the parameter variations in the considered application. A parameter estimator (PE) can be constructed upon (1) and (12) as

$$\begin{aligned} \dot{\hat{\boldsymbol{\zeta}}}_{\boldsymbol{p}}(t) &= \boldsymbol{A_p}\hat{\boldsymbol{\zeta}}_{\boldsymbol{p}}(t) + \boldsymbol{\kappa}\boldsymbol{G}(\boldsymbol{p}(t) - \hat{\boldsymbol{p}}(t)) \\ &= \boldsymbol{A_p}\hat{\boldsymbol{\zeta}}_{\boldsymbol{p}}(t) + \boldsymbol{\kappa}(\dot{\boldsymbol{x}}(t) - \boldsymbol{A_\sigma}\boldsymbol{x}(t) - \boldsymbol{G}\hat{\boldsymbol{p}}(t)) \\ \hat{\boldsymbol{p}} &= \boldsymbol{C_p}\hat{\boldsymbol{\zeta}}_{\boldsymbol{p}} \end{aligned} \tag{13}$$

where $\hat{\boldsymbol{\zeta}}_{\boldsymbol{p}}$ and $\hat{\boldsymbol{p}}$ are estimates of $\boldsymbol{\zeta_p}$ and $\boldsymbol{p}$ defined respectively in (12), while $\boldsymbol{\kappa} \in \mathbb{R}^{m\times 2}$ is the observer gain vector that needs to be selected. However, a straightforward implementation of the above estimator is complicated because of the $\dot{\boldsymbol{x}}$ term in the expression for $\boldsymbol{p}$, which requires computing the derivative of measured states. To avoid this problem, we introduce a transformation $\hat{\boldsymbol{\zeta}}_{\boldsymbol{p}} \rightarrow \hat{\boldsymbol{z}}_{\boldsymbol{p}} := \hat{\boldsymbol{\zeta}}_{\boldsymbol{p}} - \boldsymbol{\kappa}\boldsymbol{x}$ in (13) following the general design framework introduced in [21] to obtain:

$$\begin{aligned} \dot{\hat{\boldsymbol{z}}}_{\boldsymbol{p}}(t) =& (\boldsymbol{A_p} - \boldsymbol{\kappa}\boldsymbol{G}\boldsymbol{C_p})\hat{\boldsymbol{z}}_{\boldsymbol{p}}(t) + (\boldsymbol{A_p} - \boldsymbol{\kappa}\boldsymbol{G}\boldsymbol{C_p})\boldsymbol{\kappa}\boldsymbol{x}(t) \\ & - \boldsymbol{\kappa}\boldsymbol{A_\sigma}\boldsymbol{x}(t) \\ \hat{\boldsymbol{\zeta}}_{\boldsymbol{p}}(t) =& \hat{\boldsymbol{z}}_{\boldsymbol{p}}(t) + \boldsymbol{\kappa}\boldsymbol{x}(t) \\ \hat{\boldsymbol{p}}(t) =& \boldsymbol{C_p}\hat{\boldsymbol{\zeta}}_{\boldsymbol{p}}(t). \end{aligned} \tag{14}$$

The parameter $\boldsymbol{\kappa}$ is selected such that $\boldsymbol{A_p} - \boldsymbol{\kappa}\boldsymbol{G}\boldsymbol{C_p}$ is Hurwitz : the estimation error dynamics is then *globally asymptotically stable*, see [1]. The design parameter $\boldsymbol{\kappa}$ is obtained via a classical pole placement strategy: as in [1], $\boldsymbol{\kappa}$ is chosen such that all the eigenvalues of $\boldsymbol{A_p} - \boldsymbol{\kappa}\boldsymbol{G}\boldsymbol{C_p}$ are placed at $-\lambda$. The value of λ is chosen bigger than α so that the estimator is faster than the switching controller to obtain good control performances. Later on in the section, we show in (21) that the higher λ is, the faster the estimate $\hat{\boldsymbol{p}}$ will converge to the actual parameter value $\boldsymbol{p}$ from its initial value $\hat{\boldsymbol{p}}(0)$ at $t = 0$.

1) Stability Analysis: To present a more realistic analysis, we consider the effect of measurement noise and unmodeled parameter variations on the designed PE. The perturbation dynamics (12) is assumed to contain lumped residual terms indicating unmodeled parts of the perturbation, and is therefore redefined as

$$\dot{\boldsymbol{\zeta}}_{\boldsymbol{p}} = \boldsymbol{A_p}\boldsymbol{\zeta_p} + \boldsymbol{\Lambda}\mathcal{H} \tag{15}$$

where $\mathcal{H}$ is the residual vector and $\boldsymbol{\Lambda}$ is the associated input matrix. Furthermore, the effect of sensor noise on state measurement is considered in (14) by replacing $\boldsymbol{x}$ with $\boldsymbol{x_m} := \boldsymbol{x}+\boldsymbol{\nu}$, where $\boldsymbol{x_m}$ is the noisy measurement and $\boldsymbol{\nu} \in \mathbb{R}^2$ is the noise vector.

Introducing a similar transformation of the form $\boldsymbol{\zeta_p} \rightarrow \boldsymbol{z_p} := \boldsymbol{\zeta_p} - \boldsymbol{\kappa x}$ used previously and taking its derivative results in

$$\begin{aligned}\dot{\boldsymbol{z}}_{\boldsymbol{p}}(t) = (\boldsymbol{A_p} - \boldsymbol{\kappa G C_p})\boldsymbol{z_p}(t) + (\boldsymbol{A_p} - \boldsymbol{\kappa G C_p})\boldsymbol{\kappa x}(t) \\ - \boldsymbol{\kappa A_\sigma x}(t).\end{aligned} \tag{16}$$

Subtracting (14) from (16), we obtain the following error dynamics in the transformed space

$$\dot{\boldsymbol{e}}_{\boldsymbol{z}} = \boldsymbol{A_z e_z} + \boldsymbol{\Lambda}\mathcal{H} - \boldsymbol{\Gamma\nu}, \tag{17}$$

where $\boldsymbol{e_z} = \boldsymbol{z_p} - \hat{\boldsymbol{z}}_{\boldsymbol{p}}, \boldsymbol{A_z} = \boldsymbol{A_p} - \boldsymbol{\kappa G C_p}$ and $\boldsymbol{\Gamma} = (\boldsymbol{A_p} - \boldsymbol{\kappa G C_p})\boldsymbol{\kappa} - \boldsymbol{\kappa A_\sigma}$.

In the rest of this work, parameter variations are modeled using a commonly used assumption of $\dot{\boldsymbol{p}} = 0$, i.e. slow variation of parameters with respect to time ($\boldsymbol{A_p} = \boldsymbol{0}$ and $\boldsymbol{C_p} = \boldsymbol{\Lambda} = \boldsymbol{I_2}$). Replacing the above expressions in (17), the transformed estimation error dynamics can be rewritten as

$$\dot{\boldsymbol{e}}_{\boldsymbol{z}} = \lambda \bar{\boldsymbol{A}}_{\boldsymbol{z}} \boldsymbol{e_z} + \mathcal{H} - \lambda \bar{\boldsymbol{\Gamma}} \boldsymbol{\nu}, \tag{18}$$

where λ acts as the high-gain term which parameterizes the estimator gain vector $\boldsymbol{\kappa}$, $\bar{\boldsymbol{A}}_{\boldsymbol{z}} = -\bar{\boldsymbol{\kappa}}\boldsymbol{G}$ and $\bar{\boldsymbol{\Gamma}} = -\lambda\bar{\boldsymbol{\kappa}}\boldsymbol{G}\bar{\boldsymbol{\kappa}} - \bar{\boldsymbol{\kappa}}\boldsymbol{A_\sigma}$.

The ensuing stability analysis is based on the following assumptions, commonly used in literature:

Assumption 1: The unmodeled parameter variations or the residual in $\dot{\boldsymbol{p}} = \mathcal{H}$ is bounded in the sense $\|\mathcal{H}\|_\infty \leq \mu_1 \in \mathbb{R}_{>0}$

Assumption 2: The additive measurement noise $\boldsymbol{\nu}$ is bounded such that $\|\boldsymbol{\nu}\|_\infty \leq \mu_2 \in \mathbb{R}_{>0}$ [22]

Consider a Lyapunov function $V = \boldsymbol{e_z^T P_e e_z}$ bounded as $\underline{\rho}\|\boldsymbol{e_z}\|^2 \leq V \leq \bar{\rho}\|\boldsymbol{e_z}\|^2$ where $\underline{\rho}, \bar{\rho}$ denote respectively the smallest and greatest eigenvalues of $\boldsymbol{P_e} = \boldsymbol{P_e}^T \succ 0$ which satisfies

$$\boldsymbol{P_e}\bar{\boldsymbol{A}}_{\boldsymbol{z}} + \bar{\boldsymbol{A}}_{\boldsymbol{z}}^{\boldsymbol{T}}\boldsymbol{P_e} + \boldsymbol{I_2} = \boldsymbol{0}. \tag{19}$$

Taking the derivative of V along the trajectories of (18), we obtain

$$\begin{aligned}\dot{V} \leq &-\lambda\|\boldsymbol{e_z}\|^2 + 2\sqrt{2}\|\mathcal{H}\|_\infty\|\boldsymbol{P_e}\|\|\boldsymbol{e_z}\| \\ &+ 2\lambda\|\boldsymbol{\nu}\|_\infty\|\boldsymbol{P_e}\|\|\boldsymbol{e_z}\|\|\bar{\boldsymbol{\Gamma}}\| \\ \implies \dot{V} \leq &-\lambda(1-\theta)\|\boldsymbol{e_z}\|^2 \quad \forall \boldsymbol{e_z} \in \Omega\end{aligned} \tag{20}$$

where the region $\Omega = \{\boldsymbol{e_z} \mid \|\boldsymbol{e_z}\| \geq 2\sqrt{2}(\theta\lambda)^{-1}\|\mathcal{H}\|_\infty\|\boldsymbol{P_e}\| + 2\theta^{-1}\|\boldsymbol{\nu}\|_\infty\|\boldsymbol{P_e}\|\|\bar{\boldsymbol{\Gamma}}\|\}$ and $\theta \in (0,1)$ is a selected majorization constant. The obtained lower bound for $\|\boldsymbol{e_z}\|$ is a class $\mathcal{K}$ function with respect to the inputs $\mathcal{H}$ and $\boldsymbol{\nu}$. Consequently, we can claim that (18) is *input-to-state stable* (ISS) and $\boldsymbol{e_z}$ is bounded by

$$\begin{aligned}\|\boldsymbol{e_z(t)}\| \leq &\sqrt{\frac{\bar{\rho}}{\underline{\rho}}}\max\Bigg[\|\boldsymbol{e_z}(0)\|\exp(-\lambda\alpha_1 t), \\ &\left(\frac{\alpha_2\mu_1}{\lambda} + \alpha_3\mu_2\|\bar{\boldsymbol{\Gamma}}\|\right)\Bigg]\end{aligned} \tag{21}$$

where $\alpha_1 = (1-\theta)/(2\bar{\rho}), \alpha_2 = 2\sqrt{2}\|\boldsymbol{P_e}\|/\theta$ and $\alpha_3 = 2\|\boldsymbol{P_e}\|/\theta$. It is to be noted that the preceding bound for estimation error is quite similar to the one usually obtained for high-gain observers [10], [22], [23], and it can be observed that increasing the value of λ results in better attenuation of the effects of $\mathcal{H}$. Furthermore, a closer look at the expression for $\bar{\boldsymbol{\Gamma}}$ indicates that the effect of noise on $\|\boldsymbol{e_z}\|$ is amplified with increasing λ due to the linear increase in the first term, thereby illustrating the noise amplification problem associated with observers in general. In addition, there is also the presence of switching noise (due to the second term) which generates undesirable oscillations in the estimated parameters.

2) Effect of Measurement Noise: The bounds obtained previously due to the effect of measurement noise are conservative and do not consider the filtering effect introduced by estimators, To better characterize the effect of high-frequency measurement noise on the obtained estimates, we model $\boldsymbol{\nu}$ as

$$\begin{aligned}\varepsilon\dot{\boldsymbol{w}} &= \boldsymbol{Sw} \\ \boldsymbol{\nu} &= \boldsymbol{C_\nu w}\end{aligned} \tag{22}$$

where $\boldsymbol{S} = \texttt{blkdiag}(\boldsymbol{S_1}, \ldots, \boldsymbol{S_\vartheta}), \boldsymbol{S_i} = \begin{bmatrix} 0 & \omega_i \\ -\omega_i & 0 \end{bmatrix}, \boldsymbol{C_\nu} = [\boldsymbol{I_2}, \boldsymbol{I_2}, \ldots, \boldsymbol{I_2}]$ and $\varepsilon \in (0,1)$ is a small parameter which shifts the frequencies ω_i/ε of the above harmonic generator in the high-frequency range. This type of representation can be thought of as a truncated Fourier series reconstruction of a noise signal and allows us to physically model the high-frequency noise content typically introduced in the sensed measurements during data acquisition.

Ignoring the effect of $\mathcal{H}$, the asymptotic bound for transformed estimation error can be obtained using the combined system

$$\begin{aligned}\varepsilon\dot{\boldsymbol{w}} &= \boldsymbol{Sw} \\ \dot{\boldsymbol{e}}_{\boldsymbol{z}} &= \lambda\bar{\boldsymbol{A}}_{\boldsymbol{z}}\boldsymbol{e_z} - \lambda\bar{\boldsymbol{\Gamma}}\boldsymbol{C_\nu w},\end{aligned} \tag{23}$$

following the approach used in [10], which gives

$$\lim_{t\to+\infty}|e_{zi}| \leq (\alpha_4\varepsilon\lambda + \alpha_5\varepsilon)\|\boldsymbol{w}\|_\infty, \tag{24}$$

under the assumption that $\omega_i/\varepsilon \gg \lambda$. Consequently, the asymptotic bound for $e_{\zeta i} = \zeta_i - \hat{\zeta}_i$ is obtained as

$$\lim_{t\to\infty}|e_{\zeta i}| \leq (\alpha_4\varepsilon\lambda + \alpha_5\varepsilon + \alpha_6\lambda)\mu_2 \tag{25}$$

which is devoid of any filtering as

$$\lim_{\varepsilon\to 0}\lim_{t\to+\infty}|e_{\zeta i}| \neq 0. \tag{26}$$

It is to be noted that the low-pass filtering effect is visible in (24) for the transformed error coordinates as $\lim_{\varepsilon\to 0}\lim_{t\to+\infty}|e_{zi}| = 0$. However, the additive noise component introduced while recovering the actual perturbations from $\boldsymbol{e_z}$ results in a relative degree of zero between $\boldsymbol{\nu}$ and $e_{\zeta i}$.

3) Redesigned Noise Suppressing Parameter Estimator (PE-r): As shown previously, the estimate $\hat{\boldsymbol{\zeta}}_{\boldsymbol{p}}$ (and consequently $\hat{\boldsymbol{p}}$) is directly affected by $\boldsymbol{\nu}$ as there is no filtering in the designed estimator (14). A high value of λ selected for faster reconstruction of the system parameters directly amplifies the noise component rendering the estimates useless. In order to address the noise amplification problem, we modify the estimator dynamics following the approach introduced in [10] such that the estimation error injection term is filtered via a pool of stable first-order low-pass filters. This solution avoids a complex trade-off when selecting the value of λ and provides an additional degree of flexibility for suppressing high-frequency sensor noise. The resulting estimator dynamics are obtained in the following expression:

$$\begin{aligned}
\dot{\hat{\boldsymbol{\zeta}}}_{\boldsymbol{p}}(t) &= \boldsymbol{A_p}\hat{\boldsymbol{\zeta}}_{\boldsymbol{p}}(t) + \boldsymbol{\kappa G z_r}(t) \\
\dot{\boldsymbol{\eta}}(t) &= \boldsymbol{\theta}\big[-(\boldsymbol{A_\sigma} + \boldsymbol{G\theta})\boldsymbol{x}(t) - \boldsymbol{GC_p\zeta_p}(t) - \boldsymbol{G\eta}(t)\big] \\
\dot{\boldsymbol{z}}_{\boldsymbol{i}}(t) &= \boldsymbol{\theta}\big[\boldsymbol{z_{i-1}}(t) - \boldsymbol{z_i}(t)\big],\ i = \{2, \ldots, r\} \\
\boldsymbol{z_1}(t) &= \boldsymbol{\eta}(t) + \boldsymbol{\theta x}(t) \\
\hat{\boldsymbol{p}}(t) &= \boldsymbol{C_p}\hat{\boldsymbol{\zeta}}_{\boldsymbol{p}}(t)
\end{aligned} \tag{27}$$

where $\boldsymbol{\theta} = \mathtt{diag}(\lambda_\theta, \lambda_\theta)$ is the filter gain vector parameterized in terms of λ_θ. In order to ensure that the accuracy of the designed estimator remains unaffected, the filter parameter is selected such that $\lambda_\theta = \gamma\lambda$ where $\gamma > 1$ is a tuning parameter for the filters. The parameter r, which denotes the number of first-order filters, is a design choice where higher values result in a steeper cutoff in the frequency domain. In practice, $r = 1$ often gives a sufficient level of filtering under the assumption of $\dot{\boldsymbol{p}} = \boldsymbol{0}$ unless dealing with very noisy measurements. Furthermore, higher values of r become almost necessary when the disturbance is assumed to be unstructured and of time polynomial form defined in [23]. This is due to the fact that considering a higher-order time polynomial model for the disturbance results in more noise amplification in the obtained estimates as shown in [23].

Since the error equation and the transformed estimation error bounds obtained for the designed PE are very similar to that obtained in the case of general high-gain observers, the ISS property for the proposed noise suppressing parameter estimator can be easily shown following the methodology proposed in [10]. Nevertheless, we mention the key steps and main results here for the sake of clarity.

Considering the effect of measurement noise on the sensed states, we obtain the following set of equations for the estimation error vector $\boldsymbol{e_\zeta}$ and the filtered counterparts of the estimation error injection term

$$\begin{aligned}
\dot{\boldsymbol{e}}_{\boldsymbol{\zeta}} &= \boldsymbol{A_p e_\zeta} - \boldsymbol{\kappa G z_r} + \boldsymbol{\Lambda}\mathcal{H} \\
\dot{\boldsymbol{z}}_{\boldsymbol{1}} &= \boldsymbol{\theta G}[\boldsymbol{C_p e_\zeta} - \boldsymbol{z_1}] - \boldsymbol{\Gamma_\theta \nu} \\
\dot{\boldsymbol{z}}_{\boldsymbol{i}} &= \boldsymbol{\theta}(\boldsymbol{z_{i-1}} - \boldsymbol{z_i}) \quad i = \{2, \ldots, r\},
\end{aligned} \tag{28}$$

where $\boldsymbol{\Gamma_\theta} = \boldsymbol{\theta}(\boldsymbol{G\theta} + \boldsymbol{A_\sigma})$. In line with the previous assumption of $\dot{\boldsymbol{p}} = \boldsymbol{0}$ and considering $r = 1$, we define $\boldsymbol{e_\theta} = [\boldsymbol{e_\zeta}^T, \boldsymbol{z_1}^T]^T$ to obtain

$$\dot{\boldsymbol{e}}_{\boldsymbol{\theta}} = \lambda\boldsymbol{\mathcal{F}}\boldsymbol{e_\theta} + \boldsymbol{\Lambda_\theta}\mathcal{H} - \lambda\boldsymbol{\Upsilon\nu} \tag{29}$$

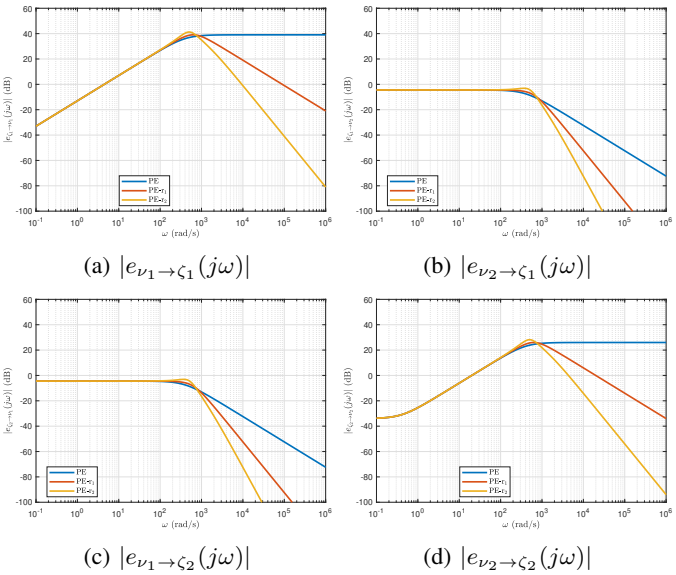

(a) $|e_{\nu_1 \to \zeta_1}(j\omega)|$ (b) $|e_{\nu_2 \to \zeta_1}(j\omega)|$

(c) $|e_{\nu_1 \to \zeta_2}(j\omega)|$ (d) $|e_{\nu_2 \to \zeta_2}(j\omega)|$

Fig. 3: Bode magnitude plots for $e_{\nu_i \to \zeta_i}(s), \quad i \in \{1, 2\}$ comparing the noise suppression capabilities of PE and PE-r with $r = \{1, 2\}$ which corroborate the theoretical results obtained in Section III.B.2 and III.B.3.

where $\boldsymbol{\mathcal{F}} = \begin{bmatrix} \boldsymbol{0} & \bar{\boldsymbol{A}}_{\boldsymbol{z}} \\ \bar{\boldsymbol{\theta}}\boldsymbol{G} & -\bar{\boldsymbol{\theta}}\boldsymbol{G} \end{bmatrix}, \bar{\boldsymbol{\theta}} = \mathtt{diag}(\gamma, \gamma), \boldsymbol{\Lambda_\theta} = \begin{bmatrix} \boldsymbol{I_2} \\ \boldsymbol{0} \end{bmatrix}, \boldsymbol{\Upsilon} = \begin{bmatrix} \boldsymbol{0} \\ \bar{\boldsymbol{\Gamma}}_{\boldsymbol{\theta}} \end{bmatrix}$, and $\bar{\boldsymbol{\Gamma}}_{\boldsymbol{\theta}} = \bar{\boldsymbol{\theta}}(\boldsymbol{G\theta} + \boldsymbol{A_\sigma})$. The obtained combined error dynamics are very similar to those obtained in (18) and hence, following the analysis performed previously for the PE in (14), we obtain upper bounds for estimation error similar to (21). This observation is also in line with that of the authors in [10], where it is shown that under the assumption of $\boldsymbol{z_1}(0) = \boldsymbol{0}$, the error bounds for observer remain unchanged.

Similarly, on analyzing the effect of measurement noise $\boldsymbol{\nu}$ on $\boldsymbol{e_\theta}$, we can obtain asymptotic bounds that match with those obtained in (24) thereby illustrating the noise suppressing capabilities of the designed parameter estimator.

4) Frequency Domain Analysis: To compare the noise-suppressing performance of the designed parameter estimators, we analyze their behavior in the frequency domain. We highlight that in our case $e_{\zeta i} = \zeta_i - \hat{\zeta}_i = p_i - \hat{p}_i$ which gives

$$\begin{aligned}
e_{\zeta_1} &= \frac{-\kappa_1}{s + \kappa_1 g_1 \mathcal{Q}_r(s)} \mathcal{Q}_r(s) \left[(s - a_{1,1}(\sigma^*))\nu_1 - a_{1,2}(\sigma^*)\nu_2\right] \\
e_{\zeta_2} &= \frac{-\kappa_2}{s + \kappa_2 g_2 \mathcal{Q}_r(s)} \mathcal{Q}_r(s) \left[(s - a_{2,2}(\sigma^*))\nu_2 - a_{2,1}(\sigma^*)\nu_1\right]
\end{aligned} \tag{30}$$

where $a_{i,j}(\sigma^*)$ are the elements of state matrix $\boldsymbol{A}(\bar{\sigma}^*)$ defined for the averaged nonlinear model under equilibrium in (4), g_i's are the diagonal elements of $\boldsymbol{G}$, κ_i's are the diagonal elements of $\boldsymbol{\kappa}$ and ν_i are the different noise components of vector $\boldsymbol{\nu}$ affecting different sensor channels and $\mathcal{Q}_r(s) = \left(\frac{\lambda_\theta}{s + \lambda_\theta}\right)^r$

is an r^{th}-order low-pass filter introduced via the estimator redesign. Clearly, selecting $r = 0$ in the above expression results in $\mathcal{Q}_r(s) = 1$ which essentially recovers the performance of PE in (14).

To further analyze the effect of noise components on the parameter estimation errors, we plug-in the values corresponding to our experimental set-up (see Table I) into (29) and analyze the following four transfer functions: $e_{\nu_i \to \zeta_i} := \frac{e_{\zeta_i}(s)}{\nu_i(s)}$, $i \in \{1, 2\}$ whose magnitude plots are obtained in Fig 3, where PE with $r = \{1, 2\}$ are denoted respectively by PE-r_1 and PE-r_2 . A few observations can be made straight away:

- Each parameter estimate is affected by noise entering via both the sensor channels used for measuring $i_L(t)$ and $v_o(t)$ which is evident from (30).
- The estimates are more affected by the principle noise component i.e. p_1 (similarly p_2) is more affected by the noise ν_1 (ν_2) entering via i_L ((v_o)) measurements as the relative degree between the estimation error and noise is r. This is clearly observed from the slope of the magnitude plots in Fig 3a and Fig 3d in the high-frequency range where noise content is expected.
- The noise entering via the cross channel is more suppressed since the relative degree is $r + 1$, evidenced by the slope of the plots in Fig 3b and Fig 3c.
- Increasing r in the redesigned estimator results in a steeper cutoff (r·20 dB/decade in principle channel and $(r + 1)$·20 dB/decade in the cross channel) in the frequency domain resulting in better noise suppression which can be observed in all the plots in Fig 3.

C. Equilibrium Point Update

The controller (7) introduced in Section III-A requires the knowledge of the equilibrium point $\boldsymbol{x^*(p)}$. Based on (4), $\boldsymbol{x^*(p)}$ is determined as:

$$\boldsymbol{x^*(p)} = \frac{1}{1 - \bar{\sigma}^*} \begin{bmatrix} p_2 + \frac{p_1}{R_o(1-\bar{\sigma}^*)} \\ p_1 \end{bmatrix}. \tag{31}$$

The parameter estimator from Section III-B provides an estimate $\hat{\boldsymbol{p}}(t)$, allowing to update the equilibrium point in real-time by combining (31) and (10) replacing $\boldsymbol{p}$ by $\hat{\boldsymbol{p}}$. The resulting expression is given by:

$$\boldsymbol{x^*(\hat{p})} = \begin{bmatrix} \frac{v_o^*}{\hat{p}_1} \left(\frac{v_o^*}{R_o} + \hat{p}_2 \right) \\ v_o^* \end{bmatrix}. \tag{32}$$

Note that, since the desired output voltage v_o^* is given by design, it is only the reference inductor current $i_L^\star(\hat{\boldsymbol{p}})$ that needs to be determined in real-time.

IV. Numerical Implementation and Experimental Validation

In this section, the strategy proposed in the previous sections is applied to a real Boost converter. Nominal circuit, controller and estimator parameters for the system considered here are given in Table I. First, simulation results are presented in order to illustrate the use of the proposed control method as well as the importance of the estimator. Then, an experimental validation is carried out to show a hardware implementation, and some interesting conclusions regarding the experimental results are drawn. A comparison with a classical controller is also proposed so as to highlight the methodological differences between the approach adopted in this paper and the more traditional PWM-based implementation of a linear controller commonly employed in power electronics.

TABLE I: Parameters used for the validation.

Parameter Type	**Parameter Value**
Circuit	$L = 4.5mH, C = 1mF, R_o = 50\Omega, i_{Load} = 0A, v_{in} = 30V, v_{in}^+ = 30V, v_{in}^- = 15V, v_o^* = 50V$
Sensor Noise	Band-limited white noise of power 10^{-10}, high-pass filtered via first-order filter with cutoff at $2\pi 10^5$
Controller & Estimator	$\alpha = 5, \boldsymbol{A_p} = \boldsymbol{0}, \boldsymbol{C_p} = \boldsymbol{I_2}, \lambda = 400, \gamma = 2.5, r = 1,$ $f_s = 5$kHz

A. Design and Implementation of Proposed algorithm

When applying the proposed technique in a digital hardware implementation, discrete sampling is required. Let T_{samp} denote the sampling period. The control and estimator design, as well as their real-time implementation, is summarized in Algorithm 1. The first part of this algorithm, shaded in red, is carried out offline and summarizes the full design procedure for control and estimation. The second part, shaded in blue, describes the code run in real time to implement both the estimator and controller designed in the first part. The goal of this online part is to determine in each time step t the mode $\sigma(t)$ to be selected. It is worth keeping in mind that the mode is held constant between two successive time steps.

Guidelines: As the choice of the parameters α, λ, γ and r is key for a successful implementation, practitioners may want to consider the following guidelines:

- Choose $\alpha = \alpha_{max}$ where α_{max} is determined as the real part of the rightmost eigenvalue of both $\boldsymbol{A}(\bar{\sigma}^*_{min})$ and $\boldsymbol{A}(\bar{\sigma}^*_{max})$. Decrease α until LMI (5) becomes feasible.
- To start with, choose $\lambda = 10\alpha$, $r = 1$, and $\gamma = 1$. Increase λ to accelerate the parameter estimation. Increase γ until the noise level in the estimated parameters is acceptable. It is to be noted that the control and estimation algorithm is designed in the continuous-time domain while the real-time implementation is in the discrete-time domain. In order to ensure that the algorithm designed in continuous-time behaves well even in the discrete-time domain, we limit the choice of observer and filter parameter to be within 10 times the sampling frequency $(1/T_{samp})$ i.e. $10 \times \gamma\lambda < 2\pi/T_{samp}$.

Following Algorithm 1, the values of v_{in}^- and v_{in}^+ are determined so as to consider unmodeled voltage drops of up to 15V in the input side. This should easily cover reductions in voltage caused by parasitic elements in the cable, inductor and IGBT module. By using the values in Table I, $\bar{\sigma}^*_{min}$ and $\bar{\sigma}^*_{max}$ have been determined to be 0.4 and 0.7, respectively. The eigenvalues of matrices $\boldsymbol{A}(\bar{\sigma}_{min})$ and $\boldsymbol{A}(\bar{\sigma}_{max})$ are given by $-10 \pm j282.7$ and $-10 \pm j141.1$, respectively. As per

Algorithm 1: Robust switching control

Input: Switched model (1), reference voltage v_o^*

Control design

Select v_{in}^+ and v_{in}^- to model possible input voltage variations
Calculate $\bar{\sigma}_{min}^* = 1 - v_{in}^+/v_o^*$
Calculate $\bar{\sigma}_{max}^* = 1 - v_{in}^-/v_o^*$
Determine $\boldsymbol{A}(\bar{\sigma}_{min}^*)$ and $\boldsymbol{A}(\bar{\sigma}_{max}^*)$
Choose α according to the desired decay rate following Remark 3
Solve LMIs (11) to find a solution $\boldsymbol{P} \succ 0$
Choose λ to be at least 10 times the value of α
Using λ, determine κ so that the eigenvalues of $\boldsymbol{A_p} - \boldsymbol{\kappa} \boldsymbol{G} \boldsymbol{C_p}$ are placed at $-\lambda$
Select $\gamma > 1$ and r to obtain a suitable noise suppression level on the estimations

Real-time implementation

Initialization : $t \leftarrow 0$, $\hat{\boldsymbol{p}}(0)$ nominal values, $\boldsymbol{x}^*$, $\sigma(0)$ (7)
while $t > 0$ **do**
    Using the measured states $\boldsymbol{x}$(t), determine $\hat{\boldsymbol{p}}(t)$ using (27)
    Update the equilibrium point $\boldsymbol{x}^*(\hat{\boldsymbol{p}}(t))$ using (32)
    Update $h(\hat{\boldsymbol{p}}(t))$ using (9)
    Calculate $s(\boldsymbol{x}(t), \hat{\boldsymbol{p}}(t))$ using (8)
    if $|s(\boldsymbol{x}(t), \hat{\boldsymbol{p}}(t))| < h(\hat{\boldsymbol{p}}(t))$ **then**
        $\sigma(t) \leftarrow \sigma(t - T_{samp})$
    else
        Determine $\sigma(t)$ as in (7)
    end
    $t \leftarrow t + T_{samp}$
end

Remark 2, the choice of $\alpha = 5$ has been made for LMIs (11) to be feasible. Following Algorithm 1, LMIs (11) are solved numerically using the Matlab Robust Control Toolbox to find a symmetric matrix $\boldsymbol{P} \succ \boldsymbol{0}$. The solution is given by:

$$\boldsymbol{P} = \begin{bmatrix} 20.13 & -0.39 \\ -0.39 & 4.47 \end{bmatrix}. \tag{33}$$

Estimator parameter λ is tuned to be faster than the convergence rate α for the switching controller while the filter parameter is selected as $\gamma = 2.5$ along with $r = 1$ to ensure that steady-state noise content in the estimates are limited to be below 0.1. In this case, the noise content is defined as the maximum deviation of the estimates from their mean steady-state values.

B. Numerical simulation

In [1], the proposed robust switching controller and parameter estimator were tested in simulation on an EV charging application scenario. Arrival or departure of EVs corresponds to steps in the load current, and the onboard BMS might impose load current ramps (when charging in constant-voltage mode for instance). For these reasons, it is proposed in this paper to consider the variations of the parameters i_{Load} and v_{in} as shown in Fig. 4, consisting of steps and ramps. Note that the changes in these parameters occur at the same time. The reason is the behavior of the voltage source, which provides a voltage value that depends on the current. More specifically, a greater input current causes a reduction in the input voltage as a protection mechanism to avoid surpassing the source current limit. In fact, here only the load current behavior is imposed. It has a direct impact on the input current which in turn modifies the input voltage, resulting in the parameter evolution shown in Fig. 4. This practical consideration should not be a problem as far as stabilization is concerned since estimates for both parameters are provided by the designed estimator. In fact, the simultaneous occurrence of both the input and load perturbations present a more stringent regulation scenario for the designed controller compared to the sequential case.

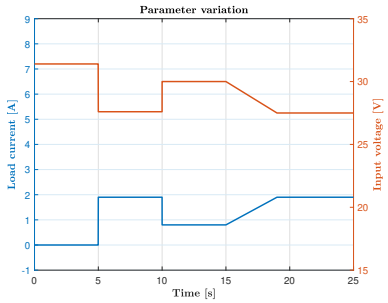

Fig. 4: Parameter variations

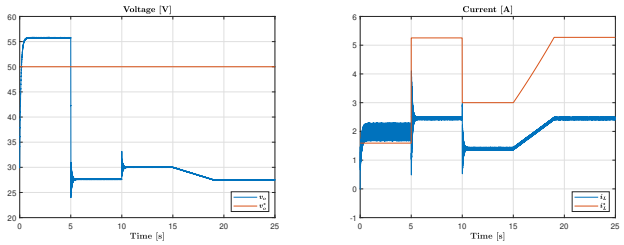

(a) Output voltage (b) Inductor current

Fig. 5: Simulation plots for ***S1***.

The simulation study is carried out in Simulink environment of MATLAB with a step time of $1\mu s$. The switching frequency of the implemented control scheme is limited to 5kHz via the hysteresis approach defined in Section III-A. A high-pass filtered white noise is added to the state variables going to the estimator designed in (27), in order to replicate the effect of measurement noise, as mentioned in Table I.

For the simulation study, two different test scenarios are considered and they are described hereafter.

[S1] Without Parameter Estimator: In this scenario, only the switching controller is implemented without the parameter estimator updating the equilibrium for $i_L^\star(t)$. Fig. 5 shows the obtained plots of the inductor current and output voltage

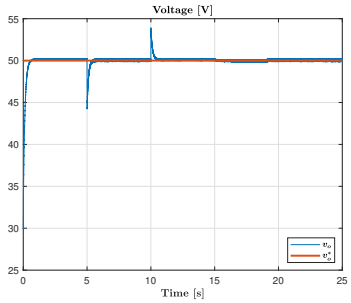

(a) Output voltage

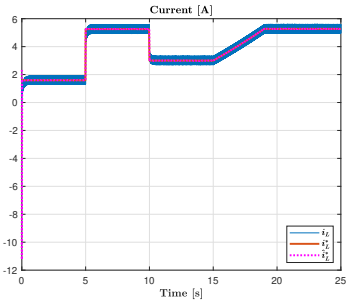

(b) Inductor current

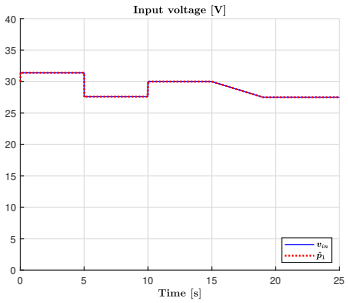

(c) v_{in} and $\hat{p}_1$

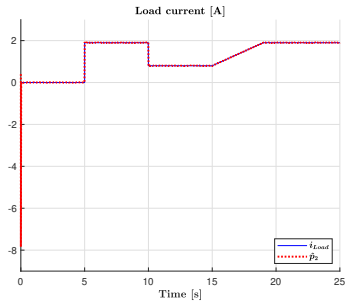

(d) i_{Load} and $\hat{p}_2$

Fig. 6: Simulation plots for ***S2***.

over time. Note that, from time instant $t = 0$, the output voltage is stabilized at about 55V instead of the reference of 50V. This is caused by the error in the input voltage, which is equal to 31.4V instead of the considered nominal value of 30V. Thus, it can be verified that even a small error of 1.4V is already sufficient to prevent stabilization at the desired operating point. Moreover, after $t = 5s$, $\boldsymbol{p}$ is such that the new voltage equilibrium value is lower than the input (30V). Since this cannot be achieved in a DBC, the system stops switching and the output voltage converges to v_{in}.

[S2] Practical Scenario with Parameter Estimator: Parametric perturbations in ***S1*** are reapplied on the closed-loop system, but now with the estimator in (27) providing the required information to update $\boldsymbol{x^*(\hat{p})}$ at each time-step. Simulation plots obtained in Fig. 6 clearly indicate that $v_o(t)$ tracks the desired reference of $v_o^* = 50V$ as the designed estimator is able to accurately reconstruct the uncertain parameters using the state measurements and the mode (σ) information which is subsequently used to update the equilibrium current i_L^*. Furthermore, the closed-loop system is able to recover from the successive simultaneous input voltage and load perturbations. Moreover, even though the assumption $\dot{\boldsymbol{p}} = \boldsymbol{0}$ does not hold when the ramp variations are applied, the estimates $\hat{\boldsymbol{p}}$ converge nonetheless to the actual perturbation values, which is evident from Figs. 6c and 6d. It is also worth noting that the estimates $\hat{\boldsymbol{p}}$ are not affected much by the measurement noise due to the additional filtering introduced in the designed estimator.

Before presenting the practical results concerning the implementation of the control strategy discussed in this paper, to be referred here as **M1**, the design of a classical PWM-based controller is presented. The latter approach shall be referred to as **M2**. The goal is to illustrate how to apply the controller proposed here in a real experimental setup and then compare it to the more traditional method, in order to highlight the differences (in terms of methodology and performance) between both approaches.

*C. PWM-based control design (**M2**)*

For comparison purposes, a classical PWM-based control design, more commonly used in practice, is also carried out. The state-space average model (3) of the Boost converter is linearized around the desired operating point, and then a classical linear controller is used in conjunction with a modulation stage such as PWM. The linearization of (3) around the equilibrium point $\boldsymbol{x^*}$ is given by:

$$\dot{\boldsymbol{\delta x}}(t) = \boldsymbol{A}(\bar{\sigma}^*)\boldsymbol{\delta x}(t) + \boldsymbol{B u}(t) + \boldsymbol{G \delta p}(t), \qquad (34)$$

where $\boldsymbol{\delta x} := \boldsymbol{x} - \boldsymbol{x^*}$, $\boldsymbol{u} := \bar{\sigma} - \bar{\sigma}^*$, $\boldsymbol{\delta p} := \boldsymbol{p} - [30 \;\; 0]^T$ (since in nominal conditions $v_{in} = 30$V and $i_{Load} = 0$) and $\boldsymbol{B} := \left[v_o^*/L \;\; i_L^*/C\right]^T$, with i_L^* also determined from the nominal parameter values. It is important to recall that this model is only valid in a neighborhood of the nominal equilibrium $\boldsymbol{x^*}$. Vector $\boldsymbol{\delta p}$ is regarded here as perturbations instead of parameters to be estimated.

A classic linear state feedback controller will be used here for the comparison. As the strategy proposed in this paper, it requires the measurements of both the inductor current and the output voltage. The control law can be expressed as follows:

$$\boldsymbol{u}(t) = -\boldsymbol{K_x}\boldsymbol{\delta x}(t) + \boldsymbol{K_i}\int_0^t \left[v_o^* - v_o(\tau)\right] d\tau, \qquad (35)$$

where $\boldsymbol{K_x}$ and K_i are control gains to be determined. Note that (35) is an extension of a PI controller where a proportional action on the current error is also considered. Considering $\boldsymbol{\delta p} = 0$, the dynamics of the augmented state $\boldsymbol{x_a} = \begin{bmatrix}\boldsymbol{\delta x}^T & x_i\end{bmatrix}^T$, with $x_i = v_o - v_o^* = [0 \;\; 1]\,\boldsymbol{\delta x}$, are given by:

$$\dot{\boldsymbol{x}}_{\boldsymbol{a}} = \overbrace{\begin{bmatrix}\boldsymbol{A}(\bar{\sigma}^*) & 0 \\ 0 \;\; 1 & 0\end{bmatrix}}^{\boldsymbol{A_a}(\bar{\sigma}^*)} \boldsymbol{x_a} + \overbrace{\begin{bmatrix}\boldsymbol{B} \\ \boldsymbol{0}\end{bmatrix}}^{\boldsymbol{B_a}} \boldsymbol{u}. \tag{36}$$

The gains $\boldsymbol{K_x}$ and K_i can be calculated by adopting the classical strategy of placing the poles of the closed-loop system matrix, which from (36)-(35) is given by $\boldsymbol{A}(\bar{\sigma}^*) - \boldsymbol{BK}$, with $\boldsymbol{K} := \begin{bmatrix}\boldsymbol{K_x}^T & K_i\end{bmatrix}^T$. For the choice of the three closed-loop poles, two of them are placed at -100rad/s and the remaining one at -1000rad/s. Note that they are much lower in magnitude than the switching frequency $\omega_s = 2\pi f_s = 3.1 \times 10^4$rad/s. The values of the gains are $\boldsymbol{K_x} = [0.11 \;\; 0.01]$ and $K_i = 1.5$.

D. Methodological comparison between *M1* and *M2*

An important conceptual difference between both methods is that, in **M1**, the switched model is used and the obtained controller stabilizes the operating point if the LMIs (11) are feasible. And this holds for any input voltage in the specified range $[v_{in}^-, v_{in}^+]$. On the other hand, in **M2**, the average model is used in order to work with a continuous model. On top of that, an approximate model based on linearization of the average model is adopted for control design. Thus, the controller is only expected to work in a neighborhood of the nominal operating point, since it is where the linearization is valid. It should be noted that the range of operating conditions in which the linearized average model is valid is not known usually.

There are also important differences between **M1** and **M2** regarding how the uncertain parameter variations are dealt with. In **M1**, these variations are estimated and then the equilibrium point is updated in order to stabilize the reference output voltage. In **M2**, no estimations are made and instead, an integral action is added in order to achieve a zero static error despite parameter variations. However, since the linearized model is used, it is not clear how to determine the ranges of parameter uncertainty that can be handled in this approach.

E. Experimental Validation

A global view of the hardware used in the experiment is shown in Fig. 7. The controller is implemented using a dSPACE platform RT1104. The IGBT module SKM50GB12T4 is used in the setup. A digital output port in the dSPACE platform is connected to a circuit board that provides the adequate voltage signal to trigger the gate of the transistor (15V). For the controller, the inductor current and the output voltage are measured using sensors and these analog signals are converted to numerical values using the analog ports of the dSPACE platform. The dSPACE platform is also connected to a computer, where the control and estimation algorithms are implemented in the software Simulink integrated with Matlab R2021b.

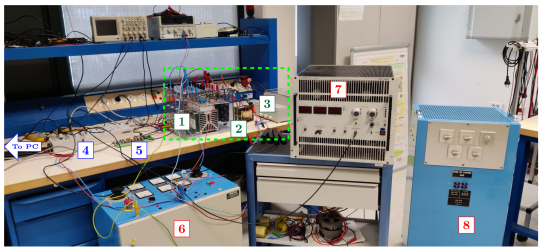

Fig. 7: Experimental setup with components: 1 - IGBT module; 2 - Inductor (L); 3 - Capacitor (C); 4 - dSPACE μC; 5 - IGBT driver circuit; 6 - Voltage source (v_{in}); 7 - Programmable load (i_{Load}); 8 - Load resistance (R_o).

*1) Method **M1**:* The plots showing the results obtained with the controller designed using **M1** are shown in Fig. 8. A low-pass filter with a crossover frequency of 100rad/s has been added to reduce the noise content in the input voltage measurements, making it easier to compare with the estimated input voltage.

Regarding the results shown in Figs. 8d and 8c, note that the estimations of the uncertain parameters obtained with the designed estimator are consistent with their real values. The estimation of i_{Load} tracks the real value, and even though there is an overshoot at start-up, it rapidly stabilizes at the correct value in a steady state. Note that no overshoots are observed in the instances where the other changes occur. In Fig. 8c, the red plot indicates the estimate of v_{in}.

It is also worth remarking that the estimations have successfully converged to the real values even while the parameters suffered ramp variations, despite assuming in the design that $\dot{\boldsymbol{p}} = \boldsymbol{0}$. The reason is that the ramp changes are sufficiently slow so that the adopted model for parameter dynamics is still considered valid and the residual $\mathcal{H}$ is comparatively very small.

Note that the estimation of v_{in}, shown in Fig. 8c, is always lower than the average measured input voltage. This can be explained by the fact that unmodeled voltage drops are also present in the real system, such as drops in the parasitic resistance of the inductor and in the semiconductor devices. Thus, the estimated input voltage corresponds in fact to the actual input voltage (which is measured in Fig. 8c) discounting all these unmodeled voltage drops. In this sense, v_{in} can be regarded here as an effective input voltage, which is even more pertinent for control purposes since in practice this is what the equilibrium point depends on. This goes to show the generality of the proposed method and its ability to address unmodeled and yet real phenomena.

The equilibrium point is updated in real-time according to the aforementioned estimations. As a result, the controller is

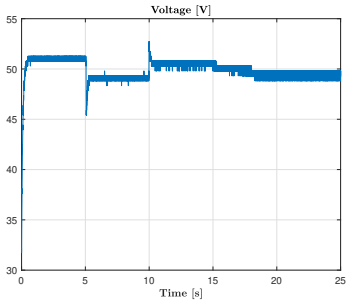

(a) Output voltage.

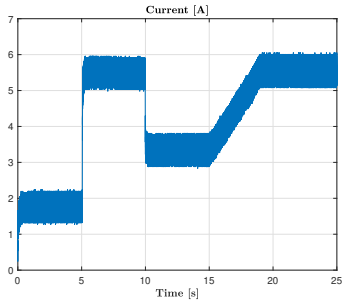

(b) Inductor current.

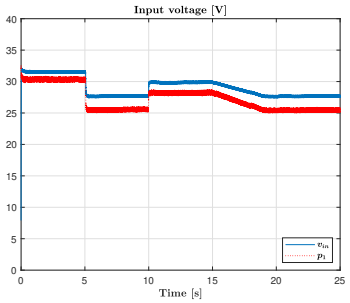

(c) Input voltage.

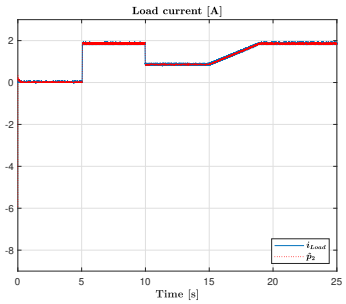

(d) Load current.

Fig. 8: Results using Method **M1**.

able to stabilize the system at the desired output voltage, as it can be seen in Fig. 8a. However, a static error can be observed in the voltage response. Furthermore, the magnitude of this error depends on the uncertain parameters, and it remains below 2% of the reference value of 50V. Therefore, it can be seen that the voltage is still in close proximity of the desired voltage. It is believed that the static error is caused by the limited sampling frequency of the dSPACE, which is 50kHz. This is suggested by the simulation result shown in Fig. 6a, where sampling is not an issue. Furthermore, it has been seen that including sampling in the simulation has the effect of introducing static errors in the voltage response. This analysis suggests that reductions in the static error, resulting in better voltage regulation, can be achieved by faster implementation using FPGA, for instance.

*2) Method **M2** :* The plots showing the results obtained with the controller designed using **M2** are shown in Fig. 9. The output voltage is indeed stabilized using Method **M2**, as seen in Fig. 9a. It is worth noting that, due to the integral action added to the state feedback controller, no static errors are observed in the voltage response. However, overshoots of about 10% occur whenever there are load step changes. The duty cycle, which in this method corresponds to the control signal, is shown in Fig. 9c.

Even though the use of **M2** has been successful in stabilizing the system with good performance regarding the elimination of the static error, it is important to note that the performance seems to be sensitive to the choice of the closed-loop system poles. Indeed, suppose that instead of placing the poles at [-100,-100,-1000]rad/s, as done in Section IV-C, the poles are placed at [-5,-5,-50]rad/s. This choice of poles corresponds to a similar performance requirement as the one imposed for **M1**, where $\alpha = 5$ was the desired decay rate. Placing the dominant poles at -5rad/s is somewhat analogous in terms of tracking convergence speed. In theory, since all poles have negative real parts, stability of the equilibrium point is still expected. However, consider the plots shown in Fig. 10, which correspond to this case. It can be seen in Fig. 10a that the output voltage is stabilized at the wrong equilibria over the course of the experiment. Indeed, the presence of large static errors can be noted in this plot, indicating that x_i diverges. This behavior is mirrored in Fig. 10c, where it is seen that the duty cycle never settles at a steady-state value and instead, it always keeps growing. One probable reason for this behavior is that, since the linearized model is used and its domain of validity is not known, placing the poles at the open left plane does not necessarily guarantee stabilization. Another factor that impacts closed-loop system stability is the initialization of the integral state, according to which this state may take longer to reach its equilibrium value x_i^*. However, it is not straightforward to determine x_i^*, implying difficulties for the choice of the initial condition for x_i. If this choice is too far away form x_i^*, large overshoots occur in the voltage response. In addition, nonlinear phenomena such as saturation of the control signal (since the duty cycle is physically constrained to be between 0 and 1) also play a role in increasing the gap between the employed linear model and the real system, making it possible for instability to occur. The aforementioned limitations reduce the interest in using the linearized model as

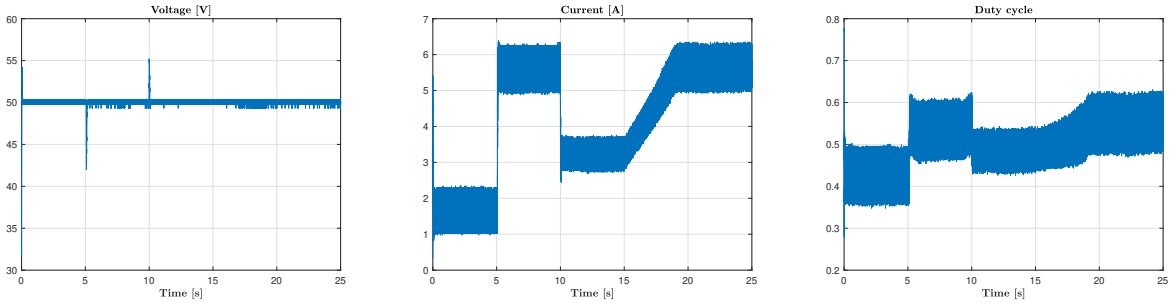

(a) Output voltage. (b) Inductor current. (c) Duty cycle.

Fig. 9: Results using Method **M2**.

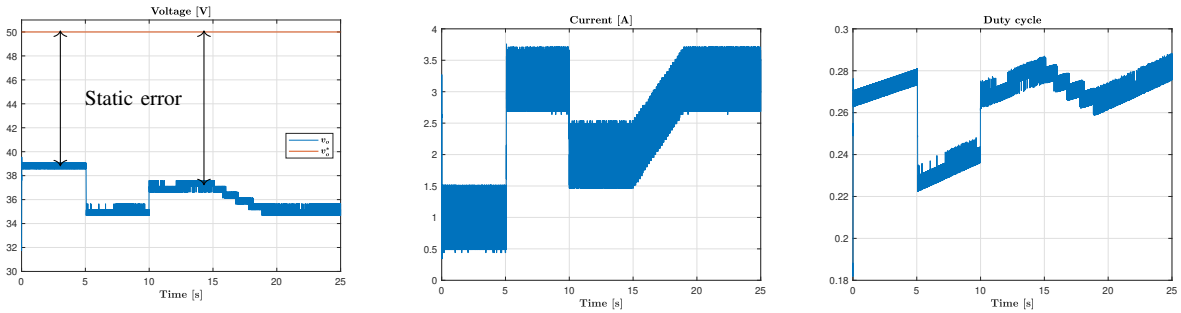

(a) Output voltage. (b) Inductor current. (c) Duty cycle.

Fig. 10: Results using Method **M2** with poles placed at [-5,-5,-50]rad/s.

a stand-in for the switched model as far as control design is concerned, depending on the pole placement selection. Since it is not easy to anticipate what choices of poles lead to unacceptable behaviors, reliability can be greatly reduced.

V. Conclusion

A robust switching controller was proposed in this work for a DC-DC boost converter operating under input voltage and load perturbations. To address the problem of uncertain equilibrium points in the context of switching controllers, a parameter estimator was constructed under the assumption that the uncertain parameters are generated via a known linear exo-system. Furthermore, the noise amplification and infinite switching frequency problems were addressed to facilitate practical implementation on real systems. Simulation results have been obtained for a real Boost converter so as to illustrate the effectiveness of the developed scheme. It has been seen that the designed estimator allows the flexibility to consider time-varying parameters characterized by linear dynamics which covers a wider class of perturbations. An experimental study has also been carried out in order to demonstrate the practical feasibility of the method presented in this paper. The main takeaway of this study is that the estimations of the uncertain parameters have been accurately obtained, making it possible to track the desired output voltage with small errors despite the technical constraints linked to the implementation, such as limited sampling. In this study, a comparison has also been made with a classical PI-type controller associated with a PWM scheme. It has been concluded that the robust switching control developed here can be more reliable since model linearization is not required and stabilization holds globally, whereas the performance of the traditional linear controller is affected by unmodeled nonlinear phenomena making it work poorly depending on the choice of the closed-loop poles.

For future works, it will be interesting to explore the effectiveness of the designed estimator for different types of parametric variations and how higher-order time-polynomial approximations for such variations affect the estimation and closed-loop performance in the context of switching controller. Furthermore, closed-loop performance of the designed estimator with other types of switching controllers, such as those designed for local stabilization, can also be investigated.

References

[1] S. Ahmad, R. P. de Souza, P. Kergus, Z. Kader, and S. Caux, "Robust switching control of dc-dc boost converter for ev charging stations," in *2023 IEEE Texas Power and Energy Conference (TPEC)*. IEEE, 2023, pp. 1–6.

[2] J. J. Justo, F. Mwasilu, J. Lee, and J.-W. Jung, "AC-microgrids versus DC-microgrids with distributed energy resources: A review," *Renewable and sustainable energy reviews*, vol. 24, pp. 387–405, 2013.

[3] T. Kobaku, S. C. Patwardhan, and V. Agarwal, "Experimental evaluation of internal model control scheme on a dc–dc boost converter exhibiting nonminimum phase behavior," *IEEE Trans. Power Electron.*, vol. 32, no. 11, pp. 8880–8891, 2017.

[4] T. Kobaku, R. Jeyasenthil, S. Sahoo, R. Ramchand, and T. Dragicevic, "Quantitative feedback design-based robust pid control of voltage mode controlled dc-dc boost converter," *IEEE Trans. Circ. Sys. II: Express Briefs*, vol. 68, no. 1, pp. 286–290, 2020.

[5] M. Bayati, M. Abedi, G. B. Gharehpetian, and M. Farahmandrad, "Sinusoidal-ripple current control in battery charger of electric vehicles," *IEEE Trans. Vehic. Techn.*, vol. 69, no. 7, pp. 7201–7210, 2020.

[6] Q. Xu, N. Vafamand, L. Chen, T. Dragičević, L. Xie, and F. Blaabjerg, "Review on advanced control technologies for bidirectional DC/DC converters in DC microgrids," *IEEE J. Emer. Selec. Topics Power Electron.*, vol. 9, no. 2, pp. 1205–1221, 2020.

[7] R. P. C. De Souza, Z. Kader, and S. Caux, "Switching control applied to interconnected boost converters: A comparison with hysteresis current control," in *2022 International Symp. Power Electronics, Electrical Drives, Automation and Motion (SPEEDAM)*. IEEE, 2022, pp. 541–546.

[8] G. Beneux, P. Riedinger, J. Daafouz, and L. Grimaud, "Adaptive stabilization of switched affine systems with unknown equilibrium points: Application to power converters," *Automatica*, vol. 99, pp. 82–91, 2019.

[9] A. Ndoye, R. Delpoux, J.-F. Trégouët, and X. Lin-Shi, "Switching control design for lti system with uncertain equilibrium: Application to parallel interconnection of dc/dc converters," *Automatica*, vol. 145, p. 110522, 2022.

[10] D. Astolfi, L. Zaccarian, and M. Jungers, "On the use of low-pass filters in high-gain observers," *Systems & Control Letters*, vol. 148, p. 104856, 2021.

[11] N. Zaupa, C. Olalla, I. Queinnec, L. Martinez-Salamero, and L. Zaccarian, "Hybrid Control of Self-Oscillating Resonant Converters With Three-Level Input," *IEEE Control Systems Letters*, vol. 7, pp. 1375–1380, 2023. [Online]. Available: https://ieeexplore.ieee.org/document/10032123/

[12] A. Sferlazza, C. Albea-Sanchez, and G. Garcia, "A hybrid control strategy for quadratic boost converters with inductor currents estimation," *Control Engineering Practice*, vol. 103, p. 104602, Oct. 2020. [Online]. Available: https://www.sciencedirect.com/science/article/pii/S0967066120301799

[13] A. Sferlazza, C. Albea-Sanchez, L. MartÃnez-Salamero, G. GarcÃa, and C. Alonso, "Min-Type Control Strategy of a DCâDC Synchronous Boost Converter," *IEEE Transactions on Industrial Electronics*, vol. 67, no. 4, pp. 3167–3179, Apr. 2020, conference Name: IEEE Transactions on Industrial Electronics. [Online]. Available: http://ieeexplore.ieee.org/abstract/document/8683986

[14] L. Hetel, M. Defoort, and M. Djemai, "Binary Control Design for a Class of Bilinear Systems: Application to a Multilevel Power Converter," *IEEE Transactions on Control Systems Technology*, vol. 24, no. 2, pp. 719–726, Mar. 2016. [Online]. Available: http://ieeexplore.ieee.org/document/7210158/

[15] R. P. C. d. Souza, "Control of networked switched systems," PhD thesis, UniversitÃ© Paul Sabatier - Toulouse III, Dec. 2023.

[16] F. Blaabjerg, *Control of Power Electronic Converters and Systems*, elsevier science ed., 2018, vol. 1.

[17] S. Oucheriah and L. Guo, "Pwm-based adaptive sliding-mode control for boost dc–dc converters," *IEEE Transactions on industrial electronics*, vol. 60, no. 8, pp. 3291–3294, 2012.

[18] M. Ahmeid, M. Armstrong, S. Gadoue, M. Al-Greer, and P. Missailidis, "Real-time parameter estimation of dc–dc converters using a self-tuned kalman filter," *IEEE Transactions on Power Electronics*, vol. 32, no. 7, pp. 5666–5674, 2016.

[19] P. Bolzern and W. Spinelli, "Quadratic stabilization of a switched affine system about a nonequilibrium point," in *Proc. 2004 American Control Conf.*, Boston, MA, USA, 2004, pp. 3890–3895.

[20] M. Doré, Y. Ariba, and G. Garcia, "General methodology for observer-based control of power electronic converters with measured perturbations," in *IEEE Conference on Control Technology and Applications (CCTA)*, 2023, pp. 1060–1065.

[21] W.-H. Chen, "Disturbance observer based control for nonlinear systems," *IEEE/ASME Trans. Mech.*, vol. 9, no. 4, pp. 706–710, 2004.

[22] S. Ahmad and H. Ahmed, "Robust intrusion detection for resilience enhancement of industrial control systems: An extended state observer approach," *IEEE Transactions on Industry Applications*, vol. 59, no. 6, pp. 7735–7743, 2023.

[23] S. Ahmad and A. Ali, "On active disturbance rejection control in presence of measurement noise," *IEEE Trans. Ind. Electron.*, vol. 69, no. 11, pp. 11 600–11 610, 2021.

Saif Ahmad received his B.Tech degree in electrical engineering from National Institute of Technology Patna, India, in 2014 and Ph.D. in electrical engineering from Indian Institute of Technology Patna, India, in 2021. From 2022 till 2023, He was a postdoc researcher at laboratory in Toulouse, France. He is currently a CNRS postdoc researcher at LIS laboratory (CNRS UMR 7020), Marseille, France. His research interests include disturbance estimation-based control, robust control of power converters, EV charging, energy management and optimization in network of renewable energy systems.

Ryan P. C. de Souza received electrical engineering degrees from both the Federal University of Rio de Janeiro (UFRJ), Brazil, and École Supérieure d'Électricité (Supélec), Gif-sur-Yvette, France, in 2019, as well as an MSc in automatic control from COPPE-UFRJ in 2020. He received his PhD in automatic control from the University of Toulouse in 2023. Currently, he is a postdoctoral researcher at LAPLACE laboratory in Toulouse, France. His research interests include hybrid systems, discrete-event systems and control of power converters.

Pauline Kergus received her engineering degree from Ecole Centrale de Lyon, France, in 2016, and her PhD in automatic control from Université de Toulouse in 2019. From 2020 to 2021, she held a postdoctoral position at LTH (Lund, Sweden) in the Department of Automatic Control. Since 2022, she is a CNRS researcher at LAPLACE, in the CODIASE group. Her research revolves around modelling, control and analysis of energy systems.

Zohra Kader received her Master of Research degree in 2014, and her PhD degree in applied mathematics in 2017, both from Université Lille 1. From 2017 to 2019, she held a Posdoctoral position at Laboratoire des Signaux et SystÃ¨mes (L2S). Since 2019, she is Associate Professor at ENSEEIHT, in Toulouse, member of the CODIASE research group at LAPLACE. Her research interests focus on control and observers design for dynamical systems with applications to modern power systems.

Stéphane Caux was born in 1970. He received the Ph.D. degree in robotics from the University of Montpellier II, France, in 1997. Since 1998, he has been an Assistant Professor with the Université de Toulouse, France, where he is currently a Professor with LAPLACE (UMR 5213 CNRS/INPT/UPS). His main research interests include robust control and observers for electrical systems (electrical motors, inverters, and fuel cell systems), and real-time energy management for multisource electrical systems (optimization method and fuzzy management).